Far-Field Optical Nanoscopy
Stefan W. Hell
Science **316**, 1153 (2007);
DOI: 10.1126/science.1137395

This copy is for your personal, non-commercial use only.

If you wish to distribute this article to others, you can order high-quality copies for your colleagues, clients, or customers by clicking here.

Permission to republish or repurpose articles or portions of articles can be obtained by following the guidelines here.

The following resources related to this article are available online at www.sciencemag.org (this information is current as of October 22, 2014):

Updated information and services, including high-resolution figures, can be found in the online version of this article at:
http://www.sciencemag.org/content/316/5828/1153.full.html

Supporting Online Material can be found at:
http://www.sciencemag.org/content/suppl/2007/05/22/316.5828.1153.DC1.html

A list of selected additional articles on the Science Web sites **related to this article** can be found at:
http://www.sciencemag.org/content/316/5828/1153.full.html#related

This article **cites 53 articles**, 16 of which can be accessed free:
http://www.sciencemag.org/content/316/5828/1153.full.html#ref-list-1

This article has been **cited by** 313 article(s) on the ISI Web of Science

This article has been **cited by** 92 articles hosted by HighWire Press; see:
http://www.sciencemag.org/content/316/5828/1153.full.html#related-urls

This article appears in the following **subject collections:**
Biochemistry
http://www.sciencemag.org/cgi/collection/biochem

Downloaded from www.sciencemag.org on October 22, 2014

Science (print ISSN 0036-8075; online ISSN 1095-9203) is published weekly, except the last week in December, by the American Association for the Advancement of Science, 1200 New York Avenue NW, Washington, DC 20005. Copyright 2007 by the American Association for the Advancement of Science; all rights reserved. The title *Science* is a registered trademark of AAAS.

36. M. Sotomayor, K. Schulten, *Science* **316**, 1144 (2007).
37. E. Evans, *Annu. Rev. Biophys. Biomol. Struct.* **30**, 105 (2001).
38. G. I. Bell, *Science* **200**, 618 (1978).
39. For adhesive interactions important in soft tissues and organs of eukaryotic cell systems, the average times t_{off}° reported for spontaneous dissociation of ligand/receptor bonds range from a fraction of a second to 100 s or more.
40. Because of thermal activation, the appropriate unit for "bond strength" is the pN. This scale follows from the ratio of thermal energy k_BT ($\sim 4.1 \times 10^{-21}$ J = 4.1 pN/nm at room temperature) to the nanometer length x_β gained in surpassing an activation-energy barrier (Fig. 1). A force of 10 pN is close to one-billionth of a gram weight (that is, 1 pN $\approx 10^{-10}$ g wt).
41. C. Wülfing, M. M. Davis, *Science* **282**, 2266 (1998).
42. E. Evans, K. Ritchie, *Biophys. J.* **72**, 1541 (1997).
43. Extending the duration of a ligand-receptor bond by a factor of 100 requires a modest collective increase of 4 to 5 k_BT in the height of the activation-energy barrier that impedes dissociation. Yet, the added persistence appears to be accompanied by a concomitant decrease in sensitivity to stress rate (lower slope f_β), suggesting that the energy landscape changes to increase the length gained in the direction of force when the bond breaks. Advanced computational methods like the "steered molecular dynamics" described in the companion review by Sotomayor and Schulten (*36*) provide valuable tools for investigating how variations in chemical structure affect activation energy barriers and pathways governing bond strength.
44. In typical laboratory tests of single adhesion bonds, constructs of the ligand and receptor molecules are chemically immobilized on solid surfaces at very low surface densities, for example, a ligand to the face of an ultrasensitive force probe and its receptor to a solid target held by a feedback-stabilized piezo translator. The target is then repeatedly moved to/from contact to the probe face, during which time the deflection of the probe is tracked at high precision and multiplied by its "spring" constant κ_f (pN/nm) to report the force history $f(t)$. Bond events are identified by the cycles showing periods of probe stretch ending in precipitous recoil, as sketched in Fig. 2A.
45. E. Evans, A. Leung, V. Heinrich, C. Zhu, *Proc. Natl. Acad. Sci. U.S.A.* **101**, 11281 (2004).
46. E. Evans, K. Kinoshita, in *Methods in Cell Biology: Cell Mechanics, Vol. 83*, Y. L. Wang, D. E. Discher, Eds. (Elsevier, New York, 2007), chap. 16.
47. E. Perret, A. Leung, H. Feracci, E. Evans, *Proc. Natl. Acad. Sci. U.S.A.* **101**, 16472 (2004).
48. M. V. Bayas, A. Leung, E. Evans, D. Leckband, *Biophys. J.* **90**, 1385 (2006).
49. Acting as a soft spring linked in series with the probe spring κ_f, the elastic response of the cell cortex κ_{cell} reduces the force rate r_f relative to the probe rate $\kappa_f v_{\text{pull}}$. The ratio $c_{rf} = r_f/(\kappa_f v_{\text{pull}})$ provides a direct assay of the cell cortical stiffness, that is, $\kappa_{\text{cell}} \approx \kappa_f c_{rf}/(1 - c_{rf})$. It is important to note that different cell types possess very different levels of interfacial stiffness and that these levels often change with cell activation or spreading on a stiffer substrate.
50. As lipid material flows onto a tether, bilayer-spanning proteins (especially those that interact with the cytoskeleton) are expected to remain behind in the cell membrane. However, the acylated proteins bound weakly to the bilayer could build up at the base of the tether, causing some to be expelled from the surface when approaching the tether-cell junction.
51. V. Heinrich, A. Leung, E. Evans, *Biophys. J.* **88**, 2299 (2005).
52. E. Evans, V. Heinrich, A. Leung, K. Kinoshita, *Biophys. J.* **88**, 2288 (2005).

53. Supported by grants from the National Institutes of Health.

10.1126/science.1137592

REVIEW

Far-Field Optical Nanoscopy

Stefan W. Hell

In 1873, Ernst Abbe discovered what was to become a well-known paradigm: the inability of a lens-based optical microscope to discern details that are closer together than half of the wavelength of light. However, for its most popular imaging mode, fluorescence microscopy, the diffraction barrier is crumbling. Here, I discuss the physical concepts that have pushed fluorescence microscopy to the nanoscale, once the prerogative of electron and scanning probe microscopes. Initial applications indicate that emergent far-field optical nanoscopy will have a strong impact in the life sciences and in other areas benefiting from nanoscale visualization.

Despite the enormous advancements brought about by electron and scanning probe microscopy, about 80% of all microscopy investigations in the life sciences are still carried out with conventional lenses and visible light. Taking advantage of the optical transparency of cells, light microscopy uniquely provides noninvasive imaging of the interior of cells in three dimensions (3D). Moreover, it allows the detection of specific cellular constituents, such as proteins, nucleic acids, and lipids, through fluorescence tagging. Lens-based fluorescence microscopy would be almost ideal for investigating life at the subcellular level if it could discern details below a quarter of a micrometer. However, since the work of Abbe, such a resolution seemed entirely out of reach, at least until recently.

When focusing a propagating beam of light, the lens ensures that the light wave interferes constructively at a point in space. The result is an intensity pattern $I(x, y, z)$ featuring a main "diffraction" maximum, referred to as the focal spot (Fig. 1A). The full width at half maximum of the spot is given by $\Delta r \approx \lambda/(2n \sin \alpha)$ in the focal plane and by $\Delta z \approx \lambda/(n \sin^2 \alpha)$ along the optical axis (*1*), with λ, α, and n denoting the wavelength, the aperture angle of the lens, and the refractive index, respectively (Fig. 1A). Because all fluorescence markers within this spot are illuminated simultaneously, they also emit at about the same time, which makes their separation virtually impossible. Moreover, the collection of the photons by a lens and their propagation to a detector are governed by a similar function, $I_{\text{em}}(x, y, z)$, blurring the coordinate from where each photon was emitted. Thus, for some time, the only pathway to subdiffraction resolution seemed to be given by near-field optical microscopy, which detects nonpropagating light waves from the sample surface with a nanosized mechanical tip (*2*). However, this method is surface-bound and cannot image the interior of cells. Similar arguments apply to the more recent and intriguing concept of imaging with a material of negative refractive index (*3*). Although such a material can project an image at a distance (*4*, *5*), the need to collect nonpropagating waves requires the sample to be placed on top of the material; a lens of negative refractive index is "near-sighted" (*6*). In many applications, especially in the life sciences, collecting the light far away from the sample is mandatory.

In the 1990s, the first concrete and feasible concepts emerged showing that in fluorescence microscopy the diffraction barrier can be broken even with propagating light and regular lenses—that is, in the far-field (*7*, *8*). A hallmark of these concepts was use of the molecular states of the fluorescent marker not just for signal generation, but also for overcoming the limits set by diffraction (*9*). They radically departed from the far-field superresolution strategies prevalent at the time, such as confocal (*10*, *11*) and multiphoton microscopy, because they implied that a resolution far below λ, in fact diffraction-unlimited resolution, is possible without eliminating diffraction per se. Meanwhile, other powerful approaches (*12*–*14*) have emerged, bolstering far-field fluorescence nanoscopy as an emerging field of science. Here, I will review this field with emphasis on the breaking of the diffraction barrier. I will refrain from overly discussing technical implementations, unless I deem them inherent to the concept; particularly, imaging speed, sensitivity, and cost-efficiency are constantly improving as new technology becomes available. Rather, I will show that all fluorescence nanoscopy concepts realized so far have used a bright and a dark state of the fluorescent marker to record sub-λ features sequentially in time. I will classify these concepts according to the states used and show that they differ on whether the sequential recording of the marker occurs molecule by molecule or in molecular ensembles.

Pushing the Diffraction Barrier

Since the mid-20th century, several concepts aimed at pushing the diffraction limits by reducing the focal spot size. Confocal fluorescence microscopy is one of them. Using pointlike illumination and detection, its effective spot is described by $I(x, y, z)I_{\text{em}}(x, y, z) \approx I^2(x, y, z)$. The

---

Department of NanoBiophotonics, Max Planck Institute for Biophysical Chemistry, 37070 Göttingen, and German Cancer Research Center (DKFZ), High Resolution Optical Microscopy Division, 69120 Heidelberg, Germany. E-mail: shell@gwdg.de

squaring reduces the spot by $\sim\sqrt{2}$, but in practice this effect is compromised by the finite detector size (*10*). A genuine quadratic dependence is provided by two-photon excitation, but exciting a fluorophore from its ground state S_0 to its fluorescent state S_1 requires photons of half the excitation energy and hence light of about 2λ in wavelength. The concomitant doubling of the spot is not compensated by the $\sim\sqrt{2}$ reduction, but even if it were, the barrier would just be shifted, not broken. These considerations are readily extended to *m* photons (*15*). Another approach shrinks the spot by an elaborate phase pattern in the entrance pupil of the lens (*16*), but giant sidelobes leave it impractical. In my view, the failure of all these concepts to provide useful improvements reinforced the notion that, ultimately, the resolution of any far-field light microscope is still bound to $\Delta r \approx \lambda/2n > 200$ nm and to merely $\Delta z \approx \lambda > 450$ nm along the optical axis.

The poorer axial resolution is particularly unfavorable for the 3D imaging of transparent samples, such as cells. The relation $\Delta z > \Delta r$ stems from the fact that a conventional lens may produce only a spherical cap of a wavefront of light (*1*). If the lens could produce a nearly complete spherical wavefront, the focal spot would be almost spherical too, because of symmetry. As a result, the *z* resolution would be similar to its lateral counterpart (*17*, *18*). The same consideration holds for fluorescence detection: The more complete the collected spherical wavefront is, the better the fluorescent marker can be located. Expanding the illumination or the detection wavefront is equivalent to increasing the aperture angle of the system. It is the key element in spot-scanning 4Pi microscopy (*18*) and widefield I^5M (*19*), both of which provide a three- to sevenfold improved *z* resolution, augmenting the 3D resolution of far-field fluorescence microscopy substantially.

To this end, 4Pi microscopy coherently adds the wavefronts of two large-angle lenses for excitation or detection, or both (Fig. 1B). The resulting main focal spot features $\Delta z \approx \lambda/3n$, which is even slightly narrower than Δr (*20*). However, because the enlarged wavefront is still not close enough to spherical ($\alpha \approx 68° < 90°$), the focal spot exhibits lobes above and below the focal plane. Consequently, practical 4Pi microscopy has relied mostly on two-photon excitation, which reduces the signal from the lobes due to the squaring effect (*20*). The remaining contributions are removed mathematically. Operating with oil, glycerol, and water-immersion lenses, two-photon 4Pi microscopy has delivered 3D images of fixed and live cells with 80- to 150-nm axial resolution (*21*). A compact beam-scanning 4Pi system recently revealed H2AX chromatin cluster formation in the nucleus (*22*), and a multispot version imaged organelles, such as the Golgi apparatus and mitochondria in live cells (*20*).

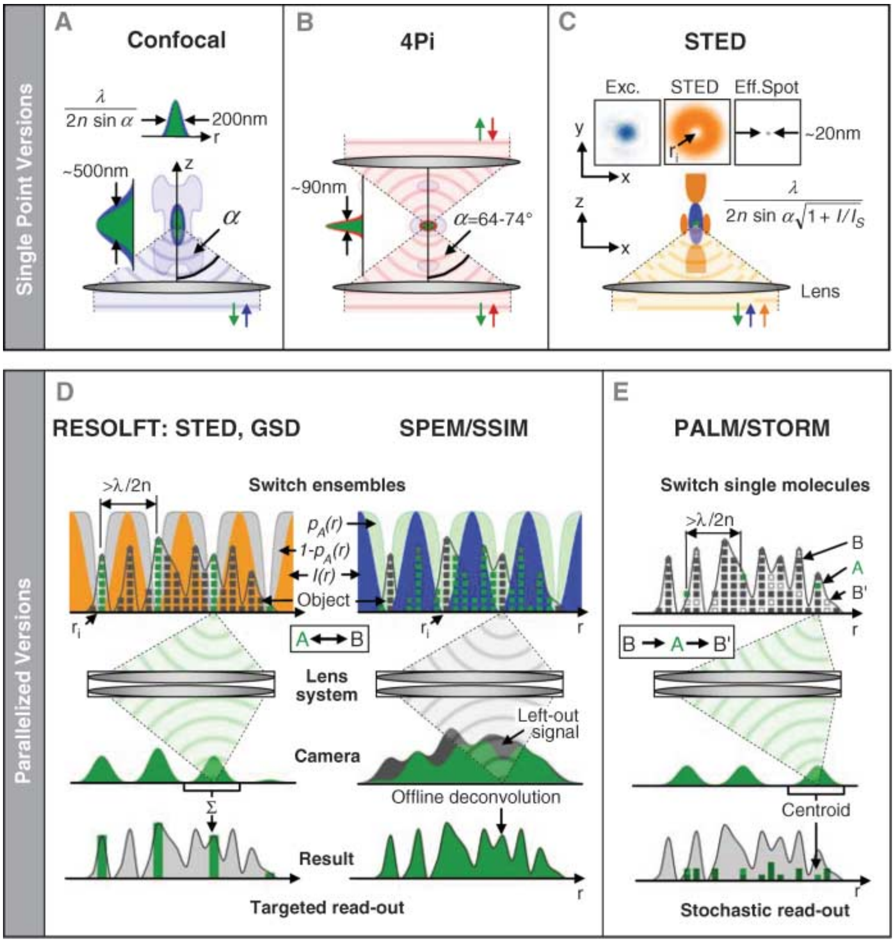

Fig. 1. Fluorescence nanoscopy schemes: single-point scanning (upper row) and parallelized versions (lower row). (**A**) Confocal microscopy. The excitation light wave (blue) formed by the lens to a spherical cap produces a 3D diffraction spot, generating fluorescence in the focal region. A pointlike detector (not shown) registers fluorescence mostly from the main maximum (shown in green), thus providing a slightly improved resolution over regular epifluorescence microscopy. Nevertheless, the confocal microscopy resolution is limited by diffraction to >200 nm in the focal plane (*x*, *y*) and to >450 nm along the optical (*z*) axis. (**B**) By combining the wavefront caps of two opposing lenses, 4Pi microscopy produces a narrower spot along the *z* axis and hence an improved *z* resolution of 80 to 150 nm. (**C**) A typical single-point scanning STED microscope uses a regularly focused excitation beam (blue) that is superimposed by a doughnut-shaped STED beam (orange) that instantly quenches excited molecules at the periphery of the excitation spot, thus confining fluorescence emission to the doughnut zero. Saturated quenching results in a fluorescent spot far below diffraction (green), here 20 nm, whose scanning across the sample yields a subdiffraction-resolution image. The spots represent measured data. (**D**) RESOLFT principle: A focal intensity distribution $I(r)$ featuring zeros that are $>\lambda/2n$ apart confines either the bright state A (left) or the dark state B (right) through a saturable or switching transition, corresponding to a parallelized STED, GSD, or photoswitching approach (on the left) and to the SPEM concept (on the right). In both cases, imaging onto a camera causes the subdiffraction features created by the bright state A (left) or the dark state B (right) at the sample to be blurred on the camera by diffraction. Left: The blur can be dealt with by summing up each diffraction blob individually and allocating the signal to the pertinent coordinate of the zero in the sample space. The image is gained by translating the zeros across the sample and reading out the fluorescence for each coordinate step. (Right) The same holds for SPEM in which the superresolved data are encoded in the narrow regions around the zeros in which the dark state B is deliberately established ("negative data set"). The image is obtained by mathematically converting the negative data set into a positive one. Both strategies rely on a targeted signal readout based on preset positions of the zeros, and both operate with fluorophore ensembles; $p_A(r) \leq 1$ defines the normalized probability of occurrence of A. Small boxes symbolize molecules making up the object (gray-shaded mountains). (**E**) PALM and STORM read out the fluorophore molecules stochastically; the molecules must be switchable. Weak illumination sparsely switches individual fluorophores to the bright state A so that they are further apart than $\lambda/2n$. Detection of $N >> 1$ photons enables the centroid calculation of the diffraction blob of individual fluorophores on the camera, and hence assembling an image with resolution depending on *N*. Concepts (C) to (E) are not diffraction-limited, meaning that they can resolve similar molecules at nanometer distances. The STED, PALM, SPEM, and RESOLFT recording process is sketched in movies S1 to S4.

By providing 6° more angle than their predecessors, the most recent field-corrected oil-immersion lenses ($\alpha = 74°$) have now also enabled bright dual-color 4Pi recordings with standard single-photon excitation (*23*, *24*). Applying two-photon excitation with such a lens pair yields a solitary central spot of $\Delta z \sim \lambda/3n$ and hence an all-physical *z*-resolution improvement (Fig. 4A) (*25*).

In I^5M, the aperture enhancement is implemented just for the detection (*26*) while the whole field of view is illuminated with a set of plane-parallel standing waves. Single-photon excitation provides a bright signal, but the flat standing-wave illumination gives rise to larger lobes requiring a more elaborate computational removal (*20*). The future implementation of 74° lenses and of special illumination schemes should render I^5M an interesting alternative to 4Pi imaging. In any case, the difference made by adding 6° to α underscores that in both concepts, the essential element is the enlargement of the aperture angle of the system (*27*). For the time being, combining the spherical wavefront caps of opposing lenses provides the smallest diffraction spot in the far-field. As a generic development, it may well augment the axial resolution of other light microscopy contrast modes in the future. Nonetheless, it does not break the diffraction barrier but rather pushes diffraction to its limits.

Breaking the Diffraction Barrier

Discerning features that are spectrally disparate is not challenged by diffraction. Likewise, Abbe's barrier does not prevent finding out the coordinate of a molecule with arbitrary precision, e.g., of 1 nm (*28*), if there is no other similar marker molecule within $\lambda/2n$ distance. Breaking Abbe's barrier is about discerning an arbitrary number of densely packed and similarly labeled features within any distance $<\lambda/2n$. This is possible if the features can be recorded sequentially: for example, by successively transferring the markers of each feature to a signal-giving "bright" state A, while keeping the other markers in a state B that is "dark" (*29*, *30*). Reading out the bright ones allows assembly of a subdiffraction image, provided that one knows their coordinate (Fig. 2).

The most direct way to determine the coordinate of the bright molecules is to define their location: r_i. This is possible by applying an optical transition A→B that would send all fluorophores to the dark state B except for those that happen to be at r_i (*29*). Such a transition can be realized by means of a light-intensity distribution $I(r)$ featuring a zero at r_i. Driving A→B, this intensity $I(r)$ must produce a rate $k_{AB}(r) = \sigma I(r)$ that outperforms competing spontaneous rates basically everywhere except at r_i. The competing spontaneous rates are given by the inverse of the lifetimes $\tau_{A,B}$ of the states A and B, respectively, and σ denotes the optical cross-section of the transition. Therefore, applying $I(r) >> (\sigma\tau_{A,B})^{-1} \equiv I_s$ fulfills this condition and confines the possible occurrence of state A to intervals $r_i \pm \Delta r/2$, with $\Delta r << \lambda/2n$. The "saturation intensity" I_s is a measure of the intensity needed to outperform the competing transitions. Translating Δr across the diffraction-blurred zone precludes a signal from any feature except from that lying within $r_i \pm \Delta r/2$, with the result that nearby features are sequentially mapped out with resolution Δr (*29*, *31*). The zeros r_i need not be moved further than $\lambda/2n$, because at $\sim r_i + \lambda/2n$, another zero can resolve the adjacent diffraction zone (*29*); that is, the process can be parallelized (Fig. 1D).

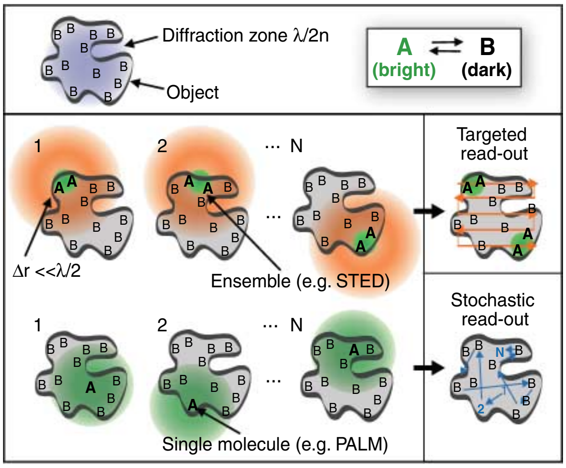

Fig. 2. Targeted versus stochastic time-sequential readout of fluorophore markers of a nanostructured object within the diffraction zone whose lower bound is given by $\lambda/2n$. A and B denote a bright and a dark state, respectively. In the targeted readout mode, one of the two states (here A) is established at a subdiffraction-sized spot at the position of a zero to read out an unknown number of fluorophore molecules. The image is assembled by deliberate translation of the zero. The zero can also be a groove. In the stochastic readout mode, a single switchable fluorophore from a random position within the diffraction zone is switched to a stable state A, while the other molecules remain in B. The coordinate is calculated from the centroid of the diffraction fluorescence spot measured by a pixelated detector. The coordinate pops up stochastically depending on where the interrogated marker molecule is located.

Time-sequential readout from within the diffraction zone at defined coordinates is a hallmark of stimulated emission depletion (STED) (*7*) and ground state depletion (GSD) microscopy (*8*), and of other concepts exploiting reversible saturable or photoswitchable transitions A ↔ B (*29*), such as saturated pattern excitation microscopy (SPEM) (*32*, *33*). These approaches have been generalized under the acronym RESOLFT (*34*), which stands for reversible saturable optically linear fluorescence transitions. With I_{max} denoting the intensity bordering the zero, their practical resolution is well approximated by

$$\Delta r \approx \frac{\lambda}{2n\sin\alpha\sqrt{1+I_{max}/I_s}}$$

which differs from Abbe's equation in that $I_{max}/I_s \rightarrow \infty$ implies "infinite" resolution, i.e., down to a molecule (*7*, *29*, *31*, *35*). The square-root factor stems from the parabolic approximation of ordinary intensity zeros in space. Fluorophores within Δr remain indiscernible because they still are simultaneously recorded. Although it can resolve single molecules (*35*), the RESOLFT concept principally operates with molecular ensembles and with state population probabilities. Δr and the average number of simultaneously recorded fluorophores can be tuned through I_{max}/I_s. The concept has been extended to also exploit the dynamic equilibration of the two states (*36*). Ultimately, the resolution is determined by the actual choice of A and B, which can be basic electronic states, such as the S_0 and the S_1, or "chemical" states such as conformational or binding states of the marker (*29*–*31*).

STED microscopy, which can be regarded as the first concept of the RESOLFT type, uses the most elementary states possible: the S_1 as A and the S_0 as B (Fig. 3). Most implementations of this concept have so far used a focused excitation beam and a red-shifted, doughnut-shaped "STED beam" for quenching excited fluorophores by stimulated emission $S_1 \rightarrow S_0$. The few stimulated photons are discarded, as is the stimulating beam. To confine the fluorescence to the zero of the doughnut, the quenching rate outperforms the spontaneous decay of the S_1 given by its inverse lifetime $\tau_{fl} \approx 10^{-9}$ s. With $\sigma \approx 10^{-16}$ cm^2, $I_s = (\sigma\tau_{fl})^{-1}$ typically amounts to 3×10^{25} photons/cm^2 s, i.e., ~10 MW/cm^2. Applying $I_{max} > I_s$ yields subdiffraction fluorescent spots. Translating the zero in any direction sequentially registers the signal from subdiffraction features, thus yielding subdiffraction images (Fig. 4B).

The zero need not be formed by a doughnut, but could also be one or many grooves (Fig. 1D) (*35*) or even planes (*37*). By using a focal zero with a strong quenching peak above and beneath the focal plane (Fig. 1C), STED initially attained Δz = 100 nm with a single lens (*38*), but in combination with a 4Pi system producing a central zero, Δz = 33 to 60 nm was possible (*37*). Setting the current benchmark, these STED-4Pi combinations are likely to push the *z* resolution to <10 nm. A similar resolution Δx = 16 nm was obtained in the focal plane (*35*) with single molecules as test objects, showing that $\sim\lambda/45$ is possible in the far-field. Realizing such lateral resolution in immunofluorescence imaging has

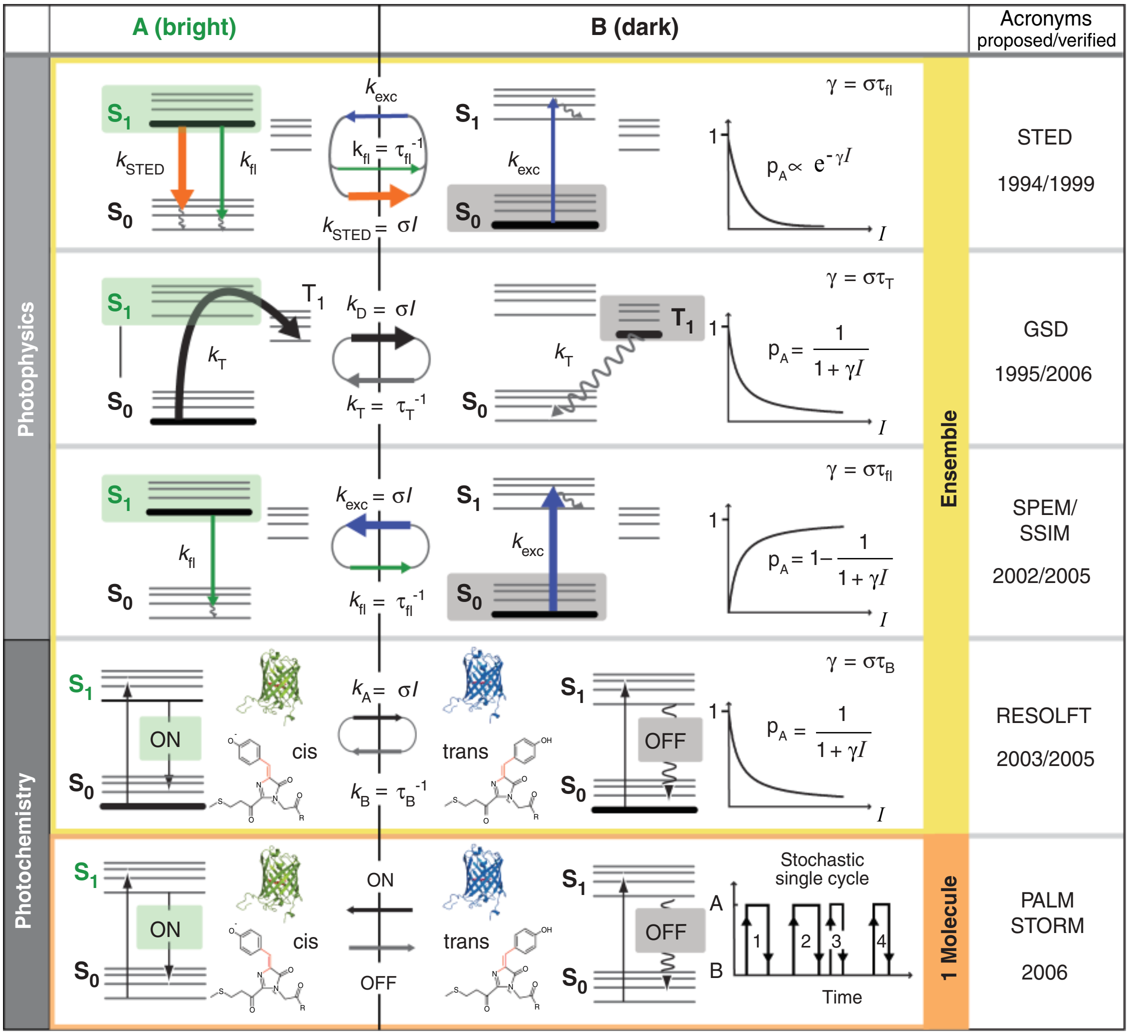

Fig. 3. Bright (**A**) and dark (**B**) molecular states used to break the diffraction barrier. Whereas STED, GSD, and SPEM utilize photophysical transitions, the photoswitching version of the RESOLFT scheme, as well as PALM and STORM, exploit photochemical transitions in which atoms are relocated or bonds formed and broken. PALM and STORM rely on measuring single (or at least identifiable) molecules at a time, whereas the other concepts, although compatible with single-molecule imaging, principally read out ensembles. Ensemble techniques rely on reversible transitions between A and B, as indicated by the rates *k*. The probability p_A of being in state A depends nonlinearly on the light intensity applied, as indicated by the equations, ensuring that either A or B is confined to a subdiffraction area at a targeted coordinate in space. The $e^{-\gamma I}$ and the $(1 + \gamma I)^{-1}$ dependence entail nonlinearities of infinite order $(\gamma I)^m$; $m \to \infty$. By increasing the lifetime of the chosen states, γ strengthens the nonlinear dependence of p_A, thus enabling huge nonlinearities at low *I*. This is radically different from *m*-photon processes that, depending on the concomitant action of *m* photons and hence just on I^m, are firmly limited to order *m* (*15*), which in practice is only $m < 4$. Because it operates with single molecules in a known state, the probability concept breaks down in PALM and STORM, but reminiscent of nonlinearity is the optical switching.

initially been hampered by photobleaching, but allowing fluorophore dark states to relax enabled $\Delta r = 20$ to 30 nm (Fig. 4C) (*39*).

Meanwhile, the nanoscale resolution provided by STED has tackled cell biology problems. For example, STED resolved synaptotagmin I from individual synaptic vesicles, showing that this protein forms isolated clusters upon vesicle fusion (*40*). STED also revealed the ringlike structure of the protein bruchpilot at synaptic active zones in the *Drosophila* neuromuscular junction (*41*). Further applications included visualizing the SNARE (soluble *N*-ethylmaleimide–sensitive factor attachment protein receptor) protein syntaxin (*42*), the nuclear protein SC35 (*39*), and the nicotinic acetylcholine receptor (*43*). STED has been extended to dual-color recording (*44*), enabling colocalized imaging on the nanoscale. Furthermore, it has revealed the spatial order of self-assembled colloidal particles (*45*) (Fig. 4B). Another application outside biology is to create nanosized spots of excited molecules that serve as the starting point for photochemical reactions (*46*).

Although STED and confocal microscopy are easily combined in the same setup, STED is not an extension of the latter, because it does not rely on a point detector. Sharp discrimination of the fluorescence signal would allow the detector to be placed right at the sample. Specifically, the resolution of a STED microscope is determined solely by the STED beam. For these reasons, parallelized STED microscopy will be possible with arrays of doughnuts or lines (Fig. 1D). Because stimulated emission is a single-photon event with a σ magnitude similar to that of absorption, the light-source requirements for STED are different from those for *m*-photon microscopy (*47*). Subnanosecond, but not femtosecond, pulses render STED effective, leaving laser diodes and photonic crystal fibers as the light sources of the future. Although the use of some fluorophores will be precluded by bleaching, suitable dyes are found in each part of the spectrum.

The S_0 and the S_1 states are not the only ones that can be exploited in this way (Fig. 3). GSD microscopy (*8*) breaks the barrier at ~100 times lower I_{max}, because it elects the metastable triplet state T_1 with a lifetime $\tau_T \approx 10^3$ to 10^6 ns as the dark state B and the singlet system (S_0 plus S_1) as A (Fig. 3). Probing A is performed at the same λ as its depletion, i.e., by pumping the dye to B. With a continuous-wave intensity of ~100 kW/cm^2, GSD has recently imaged protein clusters on the plasma membrane of fixed cells with Δr = 50- to 90-nm resolution (*48*). Although challenged by photobleaching, the ubiquity of metastable dark states in fluorophores encourages the exploration of this concept.

Depleting the S_0 state (now B) by populating the S_1 state (now A), SPEM, also known as saturated structured illumination microscopy (SSIM), differs from GSD in that ultrasharp "dark" regions of state B are created with steeply surrounded regions in which the marker, if present, is in A with high probability. Applying $I_{max} > I_s$ confines these regions to $\Delta r \ll \lambda/2n$ and conceptually yields diffraction-unlimited resolution like STED and GSD. Applying only $I_{max} < I_s$ gives the diffraction-limited resolution of an ideal confocal system (*49*). I_s is similar in magnitude to that in STED because the same molecular states are used involving the same spontaneous rates. Because it records "negative data," SPEM requires a computational construction of the image and hence an excellent signal-to-noise ratio in the raw data. Recording is performed sequentially in time by translating and rotating line-shaped zeroes that are $>\lambda/2n$ apart from each other and reading out the data with a camera. Initial realizations (*33*) displayed a lateral resolution of 50 nm with beads (after the required computation), thus also demonstrating the potential of line-shaped, quasi-widefield parallelized recording also for other A, B pairs.

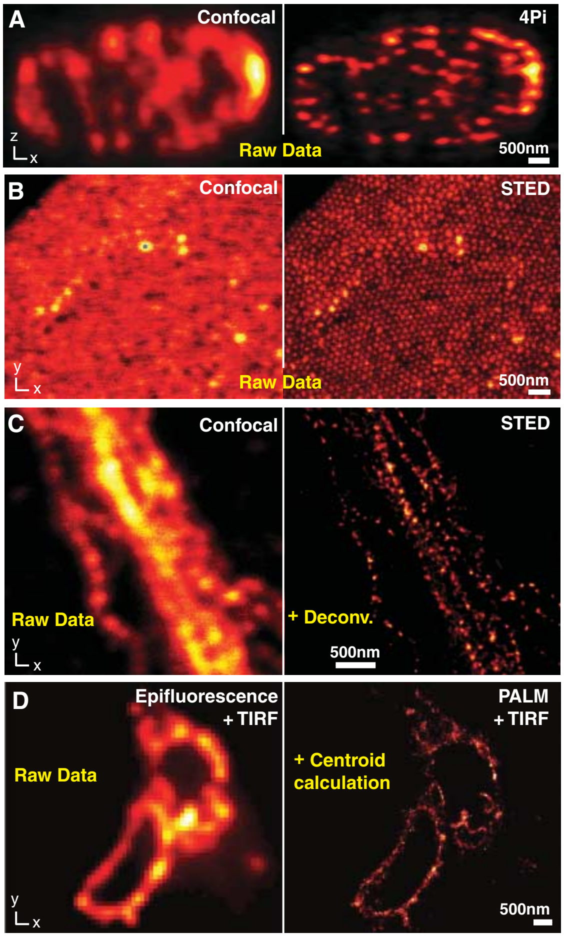

Fig. 4. Side-by-side comparisons. (**A**) Confocal versus 4Pi axial (*xz*) image of microtubules in a neuron: 4Pi image displays 140-nm *z* resolution; lens of $\alpha = 74°$ and with two-photon excitation at 800 nm. The plain 4Pi image is due to a narrow solitary peak without lobes; mathematical lobe-removal is not required. (**B**) Unlike the confocal reference, the STED image reveals the spatial order of self-assembled fused silica nanobeads containing a fluorescence core (*45*). (**C**) Neurofilaments in human neuroblastoma recorded in the confocal mode (left) and with STED after nonlinear deconvolution (right) displaying a focal plane resolution of 20 to 30 nm (*39*). (**D**) Epifluorescence versus PALM recording of a cryoprepared section from a mammalian cell expressing a lysosomal transmembrane protein tagged with a photoswitchable protein; both images were recorded with a TIRF setup. PALM resolution ranges between 20 and 60 nm, whereas individual protein localizations can be 2 nm (*12*).

The ultimate saturable transition is a photoswitch (*29*–*31*), because the absence of spontaneous interstate transitions implies $I_s \rightarrow 0$ and hence a huge I_{max}/I_s at low I_{max}. Photoswitching between isomerization or binding states, of which only A yields fluorescence, is found in reversibly photoactivatable relatives of the green fluorescent protein, such as asFP595 (*50*) and dronpa (*51*), and in photochromic synthetic compounds. The signal is gained by repeated excitation to a transient fluorescent state A↔A*. Initial experiments with asFP595 evidenced breaking Abbe's barrier by cis-trans photoisomerization with ultralow $I_{max} \approx 10$ W/cm^2 (*34*); similar results were obtained with switchable organic fluorophores (*52*). Selecting long-lived chemical states A and B highlighted that subdiffraction resolution is possible at ultralow intensities and indicated the potential of both protein and dye photoswitching for breaking Abbe's barrier (*29*–*31*). Conversely, these experiments also revealed the Achilles' heel of any concept using reversible saturable transitions, which is the finite number of cycles possible between A and B. However, cycling is required while reading out molecular ensembles from targeted coordinates with diffracted beams (Fig. 2). The reason is that ensuring state A at a chosen coordinate means that nearby molecules must be switched to B.

This problem is avoided in photoactivatable localization microscopy (PALM) (*12*, *14*) and stochastic optical reconstruction microscopy (STORM) (*13*), in which single molecules are read out from random coordinates. To this end, a single molecule is switched on or activated (B→A) such that the next activated one normally is further apart than $>\lambda/2n$; it is then repeatedly excited (A↔ A*) to render N photons forming a magnified diffraction spot on a camera. Switching off adjacent molecules is not needed because they are off (in B) already. Knowing that only a single molecule is in A allows the calculation of its coordinate from the centroid of the spot with precision $\sim\lambda/(2n\sin\alpha\sqrt{N})$. The last step is to switch off the registered molecule, or at least confirm that it is off, so that another one can be switched on and read out. Thus, the image is assembled molecule by molecule by means of a single switching cycle B→A→B′ per molecule.

PALM switches off by bleaching, implying that B may be different from B′, greatly expanding the range of useful compounds (*12*), whereas in STORM B = B′ (*13*). PALM images of thin cryosections of lysosomal transmembrane protein in a mammalian cell displayed a resolution of <25 nm (Fig. 4D). Both approaches require the adaptation of the intensity to the molecular concentration, and in both methods the resolution varies with the brightness of the molecules that are chosen to represent the object in the image. So far PALM involved recording times of hours, but with potentially 10^3 to 10^4 recorded photons per 1 ms, >1000 fluorophores from the diffraction zone could be recorded in a second with 10-nm precision in 2D (*14*). Recording with a camera provides a large field of view while impeding the imperative background rejection. For that reason, PALM was initially demonstrated with <100-nm thin sections and with a total internal reflection (TIRF) 2D recording scheme (*12*). The blur associated with defocusing single molecules should help expand the method to 3D imaging and, once background is dealt with, also to live cells.

Nanolocalization of individual fluorophores was extensively pursued in the past (*28*, *53*). Tracing the bleaching events in fluorophore clusters resolved individual molecules at nanometer distances (*54*). Likewise, individual quantum dots could be separated by disentangling their stochastic excursions to dark states (*55*). Indeed, separating and localizing individual fluorophores differing in their spectra (*56*) has been realized several times since it was proposed (*57*). It has also been known that any process allowing the allocation of N detected photons to the same point in the sample (out of the statistical evaluation of a photon stream) improves the resolution in far-field microscopy and, in fact, gives "infinite" resolution for $N\rightarrow\infty$ (*58*). However, all these precursors did not specify a definite molecular mechanism that would have enabled the sequential readout of an arbitrarily large number of fluorophores, such as the photoswitching between two states.

Most recently, nonswitching fluorophores were also used to form a B→A→B′ cycle by using a specific binding to the target cellular structure B→A and subsequent bleaching A→B′, yielding images (*59*). Complementary to the ensemble concepts, the single-molecule approaches expand the potential of nanoscale imaging. As PALM and STORM obtain their resolution in part computationally, images should be compared with those of the all-physical methods after a deconvolution. The resolution of the latter can be further increased by recording with a pixelated detector, so that both the knowledge of the preset coordinates and those from the detector could be synergistically exploited. Nonetheless, single-molecule bottom-up concepts will develop their strength at small scales and with background-free samples, whereas top-down approaches, such as STED, should be more adequate whenever background dictates registering ensembles. I expect all these methods to complement electron microscopy.

Earlier crude STED imaging of live cells (*38*) should be advanced by emergent fast beam-scanning systems. Furthermore, adjusting the mean number of simultaneously recorded fluorophores via $I_{\max}/I_s$ should meet some of the challenges posed by intracellular movements. Moreover, by providing nanosized far-field fluorescent volumes (*38*), STED should facilitate probing the dynamics of tagged biomolecules in live cells through their fluorescence fluctuations (*60*).

Although the recording speed of these concepts may differ in various applications, they must all be slower than epifluorescence microscopy. This stems from the time-sequential readout of the diffraction zone. A potential remedy is to also use other spectroscopic features, such as the emission or absorption wavelength (*57*). Indeed, state B need not be "dark," but just yield a signal different to that of A. Speed can also be gained by simultaneously installing and reading out a large number of states A, B, C, ... within the diffraction zone, either randomly or in a well-chosen order. In my view, many hurdles will be overcome by selecting the right molecular states and transitions (*9*).

In a nutshell, the diffraction barrier is broken by establishing a specific state in a region $\ll\lambda/2n$ that characterizes the features from this region (*61*). The region can be as small as, or actually be defined by, a single molecule. This state is established for a period τ within which the established spatial distribution of states is read out with the use of a suitable signal. As a rule, the shorter τ, the harder it is to read out this distribution of states. "Virtual" molecular states are not easy to use because of their transient nature ($\tau < 10^{-15}$ s). This partly explains why no effective thread has yet been described for diffraction-unlimited imaging by pure scattering or reflection. Nonetheless, virtual states could well be involved in the generation of the signal that reads out the longer-lived specific states. In any case, reflection nanoscale imaging would not automatically carry the benefits of molecular labeling and therefore could not easily unravel the biomolecular network in the cell.

A major limitation of fluorescence imaging is the limited flux of emitted photons. It is therefore important to note that none of these concepts ultimately requires fluorescence emission (*31*). Rather, it is sufficient that one of the states, say A, elicits a specific signal that can be detected. For example, if a nonfluorescent marker state A (but not B) absorbs at a particular λ, converting the absorbed photons into heat, the transient change of the refractive index of the surrounding medium could be probed with a beam of light (*62*). The measured change would still perfectly quantify the spatially confined state A. Such a nonfluorescent read-out scheme would benefit from the ultrafast (<3 ps) conversion of photons into heat, providing constant availability for absorption. It would only be limited by the sensitivity of the refractive index measurement; and maintain "multicolor" labeling through λ-specific absorption. Although the probe beam as such would be diffraction-limited, the concept would still give diffraction-unlimited resolution.

Along with improved fluorescence schemes, such nonfluorescent schemes should enable us to take another step in the not-too-distant future: nanoscale 3D imaging at high speed. In any case, the works reviewed herein already broke the barrier of perception of what a lens-based light microscope is able to accomplish. With human perseverance focused on this matter, 3D imaging of live cells with electron microscopy resolution should be possible.

References and Notes

1. M. Born, E. Wolf, *Principles of Optics* (Cambridge Univ. Press, Cambridge, 2002).
2. L. Novotny, B. Hecht, *Principles of Nano-Optics* (Cambridge Univ. Press, Cambridge, 2006).
3. J. B. Pendry, *Phys. Rev. Lett.* **85**, 3966 (2000).
4. Z. Liu, H. Lee, X. Yi, C. Sun, X. Zhang, *Science* **315**, 1686 (2007).
5. I. I. Smolyaninov, Y.-J. Hung, C. C. Davis, *Science* **315**, 1699 (2007).
6. V. A. Podolskiy, E. E. Narimanov, *Opt. Lett.* **30**, 75 (2005).
7. S. W. Hell, J. Wichmann, *Opt. Lett.* **19**, 780 (1994).
8. S. W. Hell, M. Kroug, *Appl. Phys. B* **60**, 495 (1995).
9. S. W. Hell, *Opt. Commun.* **106**, 19 (1994).
10. T. Wilson, C. J. R. Sheppard, *Theory and Practice of Scanning Optical Microscopy* (Academic Press, New York, 1984).
11. J. B. Pawley, Ed., *Handbook of Biological Confocal Microscopy* (Springer, New York, ed. 2, 2006).
12. E. Betzig *et al.*, *Science* **313**, 1642 (2006).
13. M. J. Rust, M. Bates, X. Zhuang, *Nat. Methods* **3**, 793 (2006).
14. S. T. Hess, T. P. K. Girirajan, M. D. Mason, *Biophys. J.* **91**, 4258 (2006).
15. S. W. Hell, A. Schönle, in *Science of Microscopy*, P. W. Hawkes, J. C. Spence, Eds. (Springer, New York, 2006), pp. 790–834.
16. G. Toraldo di Francia, *Nuovo Cimento* **9** (suppl.), 426 (1952).
17. Focusing of a hypothetical spherical wavefront yields a spot of about one-third of the wavelength, but not a far smaller one as was conjectured by Cremer *et al*. (*63*). So, the actual benefit is the *z*-resolution improvement.
18. S. W. Hell, E. H. K. Stelzer, *Opt. Commun.* **93**, 277 (1992).
19. M. G. L. Gustafsson, D. A. Agard, J. W. Sedat, *Proc. SPIE* **2412**, 147 (1995).
20. A. Egner, S. W. Hell, *Trends Cell Biol.* **15**, 207 (2005).
21. H. Gugel *et al.*, *Biophys. J.* **87**, 4146 (2004).
22. J. Bewersdorf, B. T. Bennett, K. L. Knight, *Proc. Natl. Acad. Sci. U.S.A.* **103**, 18137 (2006).
23. M. Lang, T. Müller, J. Engelhardt, S. W. Hell, *Opt. Express* **15**, 2459 (2007).
24. M. Lang, J. Engelhardt, S. W. Hell, *Opt. Lett.* **32**, 259 (2007).
25. M. Lang, J. Engelhardt, S.W. Hell, personal communication.
26. M. G. L. Gustafsson, D. A. Agard, J. W. Sedat, *J. Microsc.* **195**, 10 (1999).
27. By not expanding the microscope's aperture, the interference of unfocused waves from opposing lenses (*64*) produces several peaks of similar height at the focal regions, which strictly cannot superresolve (arbitrary) objects along the *z* axis.
28. C. Kural *et al.*, *Science* **308**, 1469 (2005).
29. S. W. Hell, *Nat. Biotechnol.* **21**, 1347 (2003).
30. S. W. Hell, S. Jakobs, L. Kastrup, *Appl. Phys. A* **77**, 859 (2003).
31. S. W. Hell, *Phys. Lett. A* **326**, 140 (2004).
32. R. Heintzmann, T. M. Jovin, C. Cremer, *J. Opt. Soc. Am. A* **19**, 1599 (2002).
33. M. G. L. Gustafsson, *Proc. Natl. Acad. Sci. U.S.A.* **102**, 13081 (2005).
34. M. Hofmann, C. Eggeling, S. Jakobs, S. W. Hell, *Proc. Natl. Acad. Sci. U.S.A.* **102**, 17565 (2005).
35. V. Westphal, S. W. Hell, *Phys. Rev. Lett.* **94**, 143903 (2005).
36. J. Enderlein, *Appl. Phys. Lett.* **87**, 097105 (2005).
37. M. Dyba, S. W. Hell, *Phys. Rev. Lett.* **88**, 163901 (2002).
38. T. A. Klar, S. Jakobs, M. Dyba, A. Egner, S. W. Hell, *Proc. Natl. Acad. Sci. U.S.A.* **97**, 8206 (2000).
39. G. Donnert *et al.*, *Proc. Natl. Acad. Sci. U.S.A.* **103**, 11440 (2006).
40. K. I. Willig, S. O. Rizzoli, V. Westphal, R. Jahn, S. W. Hell, *Nature* **440**, 935 (2006).
41. R. J. Kittel *et al.*, *Science* **312**, 1051 (2006).
42. J. J. Sieber, K. I. Willig, R. Heintzmann, S. W. Hell, T. Lang, *Biophys. J.* **90**, 2843 (2006).
43. R. Kellner, J. Baier, K. I. Willig, S. W. Hell, F. J. Barrantes, *Neuroscience* **144**, 135 (2007).
44. G. Donnert *et al.*, *Biophys. J.* **92**, L67 (2007).
45. K. Willig, J. Keller, M. Bossi, S. W. Hell, *N. J. Phys.* **8**, 106 (2006).
46. V. S. Letokhov, in *Ultrafast Processes in Chemistry and Photobiology*, M. El-Sayed, Ed. (Blackwell Science, Oxford, 1995), pp. 195–214.
47. W. Denk, J. H. Strickler, W. W. Webb, *Science* **248**, 73 (1990).
48. S. Bretschneider, C. Eggeling, S. W. Hell, personal communication.
49. M. G. L. Gustafsson, *J. Microsc.* **198**, 82 (2000).
50. K. A. Lukyanov *et al.*, *J. Biol. Chem.* **275**, 25879 (2000).
51. R. Ando, H. Mizuno, A. Miyawaki, *Science* **306**, 1370 (2004).
52. M. Bossi, J. Fölling, M. Dyba, V. Westphal, S. W. Hell, *N. J. Phys.* **8**, 275 (2006).
53. W. E. Moerner, *Nat. Methods* **3**, 781 (2006).
54. X. Qu, D. Wu, L. Mets, N. F. Scherer, *Proc. Natl. Acad. Sci. U.S.A.* **101**, 11298 (2004).
55. K. A. Lidke, B. Rieger, T. M. Jovin, R. Heintzmann, *Opt. Express* **13**, 7052 (2005).
56. A. M. van Oijen, J. Köhler, J. Schmidt, M. Müller, G. J. Brakenhoff, *J. Opt. Soc. Am. A* **16**, 909 (1999).
57. E. Betzig, *Opt. Lett.* **20**, 237 (1995).
58. S. W. Hell, J. Soukka, P. E. Hänninen, *Bioimaging* **3**, 64 (1995).
59. A. Sharonov, R. M. Hochstrasser, *Proc. Natl. Acad. Sci. U.S.A.* **103**, 18911 (2006).
60. L. Kastrup, H. Blom, C. Eggeling, S. W. Hell, *Phys. Rev. Lett.* **94**, 178104 (2005).
61. Conceptually, it is enough to establish a steep spatial gradient between the occurrence of at least two states, meaning that the state need not be literally "confined."
62. D. Boyer, P. Tamarat, A. Maali, B. Lounis, M. Orrit, *Science* **297**, 1160 (2002).
63. T. Cremer *et al.*, *Microsc. Acta* **81**, 31 (1978).
64. C. Bailey *et al.*, *Nature* **366**, 44 (1993).
65. I thank M. Lang and J. Engelhardt (DKFZ) for providing Fig. 4A and L. Meyer and G. Donnert for providing Fig. 4C. E. Rittweger and V. Westphal (Max Planck Institute) helped prepare the figures. I also thank G. Donnert, C. Eggeling, A. Egner, S. Jakobs, L. Kastrup, B. Rankin, V. Westphal, K. Willig, and A. Schönle for reading of the manuscript. Funding was from the Max Planck Society, Deutsche Forschungsgemeinschaft, Volkswagen Foundation, Landesstiftung Baden-Württemberg, European Union (New and Emerging Science and Technology, SPOTLITE), and German Ministry of Research and Education. The author consults for Leica Microsystems CMS Gmbh, Mannheim, Germany.

Supporting Online Material

www.sciencemag.org/cgi/content/full/316/5828/1153/DC1
Movies S1 to S4

10.1126/science.1137395